Vietnam Journal of Science and Technology
DOI: https://doi.org/10.15625/2525-2518/23961

A novel N-NiFe electrocatalyst for hydrogen production via water splitting

Lam Thi Thuy Kieu[1], Nguyen Tu Quyen[1], Truong Ngoc Cam Khuyen[1], Nguyen Nhat Tuan[1], Nguyen Duc Nhan[2], Phan Thi Thuy Trang[2], Le Thi Thanh Lieu[1], Dinh Quoc Viet[2], Vien Vo[2], Nguyen Van Thang[2,*]

[1]Faculty of Education, Quy Nhon University,
170 An Duong Vuong, Quy Nhon Nam, Gia Lai, Viet Nam
[2]Faculty of Natural Sciences, Quy Nhon University,
170 An Duong Vuong, Quy Nhon Nam, Gia Lai, Viet Nam

[*]Email: *nguyenvanthang@qnu.edu.vn*

Received: 16 December 2025; Accepted for publication: 1 March 2026

Abstract. Non-precious metal electrocatalysts for water splitting to produce hydrogen are of great interest in the context of reducing CO_2 emissions. In this study, NiFe alloy materials and their nitrogen-modified form, N-NiFe, were synthesized from the Prussian Blue $Ni_3[Fe(CN)_6]_2$ (NiFe PB) precursor for application as electrocatalysts in the hydrogen evolution reaction (HER). XRD results revealed that NiFe PB decomposed to form an fcc-structured NiFe alloy phase, while the subsequent nitrogen doping process (N-NiFe) resulted in reduced crystallinity and smaller crystal size. Electrochemical measurements demonstrated that N-NiFe exhibited superior HER performance, achieving the lowest overpotential at 10 mA cm^{-2} (468 mV), the smallest Tafel slope (171 mV dec^{-1}), and the highest double-layer capacitance (Cdl) and electrochemically active surface area (ECSA) among the investigated samples. These improvements are attributed to increased electron density, the formation of new active sites, and enhanced charge transfer capability due to nitrogen doping. The research results indicate that the N-NiFe material is a promising catalyst for water splitting to produce hydrogen.

Keywords: Prussian blue analogue, NiFe alloy, nitrogen-doped NiFe, HER electrocatalyst, water splitting.

Classification numbers: 2.4.2, 2.6.1, 2.8.2.

1. INTRODUCTION

In the context of the growing demand for clean energy, the development of sustainable energy conversion technologies plays an increasingly critical role. Among these, water electrolysis for hydrogen production is considered one of the most promising solutions to replace traditional fossil fuel sources, as hydrogen is a clean fuel with high energy density and produces no CO_2 emissions upon utilization [1]. However, the electrochemical water-splitting process involves both the hydrogen evolution reaction (HER) and the oxygen evolution reaction (OER), which require a substantial amount of electrical energy [2]. To reduce the electrical energy input for water splitting, a highly efficient and robust electrocatalyst is essential to accelerate the kinetics of both OER and HER [3]. Precious metal materials such as Pt, IrO_2, and RuO_2, while possessing high catalytic activity, are expensive and rare hinders commercial

application [4]. Consequently, the search for high-performance, durable non-precious electrocatalysts has become a major research focus in recent years.

In this context, Prussian blue analogues (PBAs), a subclass of crystalline metal-organic frameworks (MOFs) with diverse compositions and morphologies, have been extensively studied as precursors for synthesizing various functional materials [5]. The PBA-based materials possess various advantages suitable for HER catalysts, such as flexibility in transition metal replacement, high specific surface area, and homogeneous dispersion of active sites in a three-dimensional structure. The potential of these materials in the electrochemical water splitting, especially in HER, has been demonstrated [6–8]. Despite the diversity of structural and catalytic properties of PBAs, their low electrical conductivity and inactivation of the catalytic sites due to ligand coordination prohibit the electrocatalytic activity of these materials in HER applications. Therefore, strategies have been investigated including synthesis of PBAs derivatives using thermal treatment to turn PBAs into metal alloys, or metal compounds such as oxides, sulfides, phosphides [9, 10]. Accordingly, PBA-based materials have great potential in HER electrochemical catalytic applications and should be investigated more extensively.

Notably, PBA-derived metals, metal oxides/hydroxides and metal sulfides have been reported as promising electrode materials for electrochemical energy storage and conversion applications [11]. Furthermore, due to their abundance in nitrogen-containing organic ligands (CN^- groups) and transition metal cations, PBAs are regarded as promising precursors for synthesizing nitrogen-doped materials with high nitrogen content, potentially leading to the formation of metallic or alloy nanoparticles.

Alloys of 3D transition metals, such as NiFe, FeCo, and CoNi, have been demonstrated to be highly active and cost-effective for water splitting [9]. The alloying of transition metals alters the electronic structure of the constituent metal atoms due to the influence of neighboring dissimilar metal atoms, leading to optimized interaction strengths and reduced adsorption free energy of HER and OER intermediates [10]. As an example, NiFe alloys exhibit superior electrocatalytic activity compared to their monometallic Ni and Fe counterparts [12]. In NiFe alloys, the electronic structure of Ni atoms is modulated by adjacent Fe atoms, resulting in enhanced water-splitting performance [13]. However, most metal alloys, when exposed to harsh electrolyte environments, tend to be susceptible to oxidation, dissolution, and corrosion, leading to poor electrocatalytic durability [14]. Doping a non-metal element, such as nitrogen, into the NiFe lattice can significantly improve electrical conductivity and create a higher density of active sites, thereby boosting catalytic performance. Nitrogen doping effectively regulates the electronic structure of the Ni and Fe surface active sites. Due to its high electronegativity, N induces charge redistribution, which can optimize the binding energy of reaction intermediates, such as H* for HER. Specifically for HER, N-doping provides more favorable adsorption sites for H*, lowering the energy barrier for the Volmer step and thus enhancing intrinsic HER activity. In this work, the NiFe system primarily focuses on HER optimization. The nitrogen doping via urea treatment was specifically designed to address the sluggish HER kinetics often found in Ni-based alloys in acid media by creating high-density M-Nx [15].

In this study, novel nitrogen-doped NiFe alloy (N-NiFe) was synthesized via a simple thermal treatment of NiFe with urea under an inert atmosphere. The nitrogen doping process introduces lattice defects and generates new active sites, while also enhancing the material's conductivity through the formation of electron-rich regions. The results indicate that the N-NiFe material reduces the overpotential for the HER, facilitating efficient water splitting.

2. EXPERIMENTAL SECTION

2.1. Chemicals

All chemicals were used as received, including nickel sulfate hexahydrate ($NiSO_4 \cdot 6H_2O$, ≥ 98 %), potassium ferricyanide ($K_3[Fe(CN)_6]$, ≥ 99 %), ethanol (C_2H_5OH, ≥ 99.5 %), N-methyl-2-pyrrolidone (NMP, C_5H_9NO, ≥ 99 %), Nafion solution (a perfluorinated polymer resin dissolved in solvent) from Sigma Aldrich; urea (H_2NCONH_2, 99 %) and sulfuric acid (H_2SO_4) from Xilong, China.

2.2. Material synthesis

2.2.1. Prussian blue $Ni_3[Fe(CN)_6]_2$

The $Ni_3[Fe(CN)_6]_2$ material was synthesized via a co-precipitation method at room temperature. In a typical process, 20 mL of a 0.1 M Ni^{2+} solution was prepared by dissolving 1.3142 g of $NiSO_4 \cdot 6H_2O$ in distilled water. Simultaneously, 20 mL of a 0.1 M $K_3[Fe(CN)_6]$ solution was prepared by dissolving 1.6462 g of $K_3[Fe(CN)_6]$ in distilled water. The Ni^{2+} solution was added dropwise into the continuously stirred $K_3[Fe(CN)_6]$ solution to ensure uniform precipitation of $Ni_3[Fe(CN)_6]_2$. The obtained precipitate was thoroughly washed and then dried at 60 °C for 12 hours in a vacuum oven. The final blue product was denoted as PB NiFe.

2.2.2. NiFe alloy

The as-prepared PB NiFe was calcined at 700 °C under an Ar atmosphere for 2 hours with a heating rate of 10 °C min^{-1}, followed by natural cooling in the furnace. The resulting material was ground into a fine powder and denoted as NiFe.

2.2.3. Nitrogen-doped NiFe (N-NiFe)

The as-synthesized NiFe powder was thoroughly mixed with urea at a mass ratio of 1:1, ground finely, placed in a covered alumina crucible, and wrapped with aluminum foil. The mixture was then calcined at 700 °C for 2 hours under an Ar atmosphere with a heating rate of 10 °C min^{-1}. The resulting sample was washed repeatedly with water and ethanol and subsequently dried. The final material was denoted as N-NiFe.

2.3. Material characterization

X-ray diffraction (XRD) patterns of the samples were recorded on a Bruker D2 Advance diffractometer using a Cu X-ray source (Cu Kα radiation, λ = 1.5406 Å) operated at 40 kV and 40 mA. The scan range was from 2° to 80° (2θ) with a step size of 0.008° and a step time of 0.6 seconds. Fourier-transform infrared (FT-IR) spectra were recorded on an IRAffinity-1S spectrometer (Shimadzu) in the range of 400 to 4000 cm^{-1}. The surface morphology and elemental composition (via energy-dispersive X-ray spectroscopy, EDS) of the materials were examined using field-emission scanning electron microscopy (FE-SEM, JSM-IT800/JEOL).

2.4. Electrochemical measurements

The electrocatalytic properties of the materials for the HER were evaluated using a standard three-electrode electrochemical workstation (Corrtest, China). A platinum wire served

as the counter electrode (CE), an Ag/AgCl electrode (immersed in saturated KCl solution) as the reference electrode (RE), and a glassy carbon electrode coated with the prepared catalyst as the working electrode (WE). The electrolyte was a 0.5 M H_2SO_4 aqueous solution. Linear sweep voltammetry (LSV) was performed at a scan rate of 50 mV s^{-1} to obtain polarization curves (current vs. potential, I–V). Cyclic voltammetry (CV) was then conducted in a non-faradaic potential region at various scan rates to determine the double-layer capacitance (Cdl) and subsequently estimate the electrochemically active surface area (ECSA). The catalyst loading on the glassy carbon electrode was 0.235 mg cm^{-2}. The CV curves were recorded at various scan rates, including 5, 10, 20, 50, 100, and 200 mV s^{-1}. The charging current density difference, $\Delta j = (j_a - j_c)/2$ (where j_a and j_c are the anodic and cathodic current densities, respectively), was plotted against the scan rate. The *Cdl* value was then extracted from the slope of the resulting linear fit. The ECSA was subsequently calculated using the following equation: $ECSA = Cdl/Cs$, where *Cs* is the specific capacitance of a flat surface, which was assumed to be 0.035 mF cm^{-2} based on reported literature for similar systems [16].

3. RESULTS AND DISCUSSION

3.1. Material characterization

The structural characteristics of the synthesized materials were investigated by XRD, as shown in Figure 1. The XRD pattern of PB NiFe (Figure 1a) shows several moderate-intensity diffraction peaks at 2θ of 17°, 24°, 35°, 39°, 43°, 51°, 57°, and 68°, which are characteristic of the cubic crystal structure of Prussian Blue Analogue (PBA) with the space group Fm-3m (PDF Card: 00-014-0291). The high intensity and sharpness of these peaks indicate good crystallinity of the as-synthesized PBA [17]. Thermal treatment significantly altered the material structure, as evidenced by the markedly different XRD pattern of the NiFe alloy. The diffraction pattern changed dramatically, typically the characteristic PBA peaks disappeared, and new, sharp diffraction peaks corresponding to the (111), (200), and (220) planes of a face-centered cubic (fcc) $FeNi_3$ alloy appeared at 44.3°, 51.6°, and 76.1°, respectively [18]. This confirms the complete decomposition of the PBA precursor and the successful formation of a well-crystallized NiFe alloy.

For the N-NiFe sample, the XRD pattern in Figure 1b reveals that the characteristic fcc NiFe peaks ((111), (200), (220)) are retained, indicating that the fundamental alloy crystal structure was not destroyed during the nitrogen doping process. However, the diffraction peaks of N–NiFe exhibit a slight shift toward lower 2θ angles compared to pristine NiFe, suggesting a minor lattice expansion associated with the incorporation of nitrogen atoms into interstitial sites rather than substitutional positions. In addition, the N–NiFe sample shows weaker peak intensities and a broader diffraction background, indicative of reduced crystallinity and smaller crystallite size. These observations suggest that nitrogen is primarily incorporated as an interstitial and/or surface species, influencing lattice strain and crystallinity without significantly changing the overall crystal structure. Based on the Scherrer equation, the crystallite sizes of the materials were calculated to be 19.0, 4.0, and 3.5 nm for PB NiFe, NiFe, and N-NiFe, respectively.

The bonding features of the materials were examined using FT-IR spectroscopy (Figure 1). As shown in Figures 1c and 1d, the FT-IR spectra of the PB NiFe, NiFe, and N-NiFe samples (Figures 1c) show clear differences in their bonding structures. For PB NiFe, a characteristic absorption band in the ~2100–2150 cm^{-1} region corresponds to the stretching vibration of the –

C≡N group within the Prussian Blue framework (Fe–C≡N), confirming the presence of the cyanide network typical of PBAs. Simultaneously, the PB NiFe spectrum also shows a peak at ~600 cm^{-1} (Figure 1d), assigned to the Fe^{2+}–CN–Fe^{3+} bending vibration, a common feature of PBAs [19]. In contrast, NiFe, obtained after the cyanide framework removal, no longer exhibits the C≡N band, and its IR spectrum only shows weak vibrations in the low-frequency region. This demonstrates the complete collapse of the PB framework during thermal treatment and the phase transition to a Ni–Fe alloy matrix [20]. Remarkably, for the N-NiFe sample, the IR spectrum reveals a significant increase in the absorption along with vibrational bands in the wavenumber ranges of approximately 410–450 cm^{-1} and 650–750 cm^{-1} (Figure 1d). The broadening and distortion of the metal framework vibration region are considered indicative of the formation of Ni–N/Fe–N bonds [21, 22].

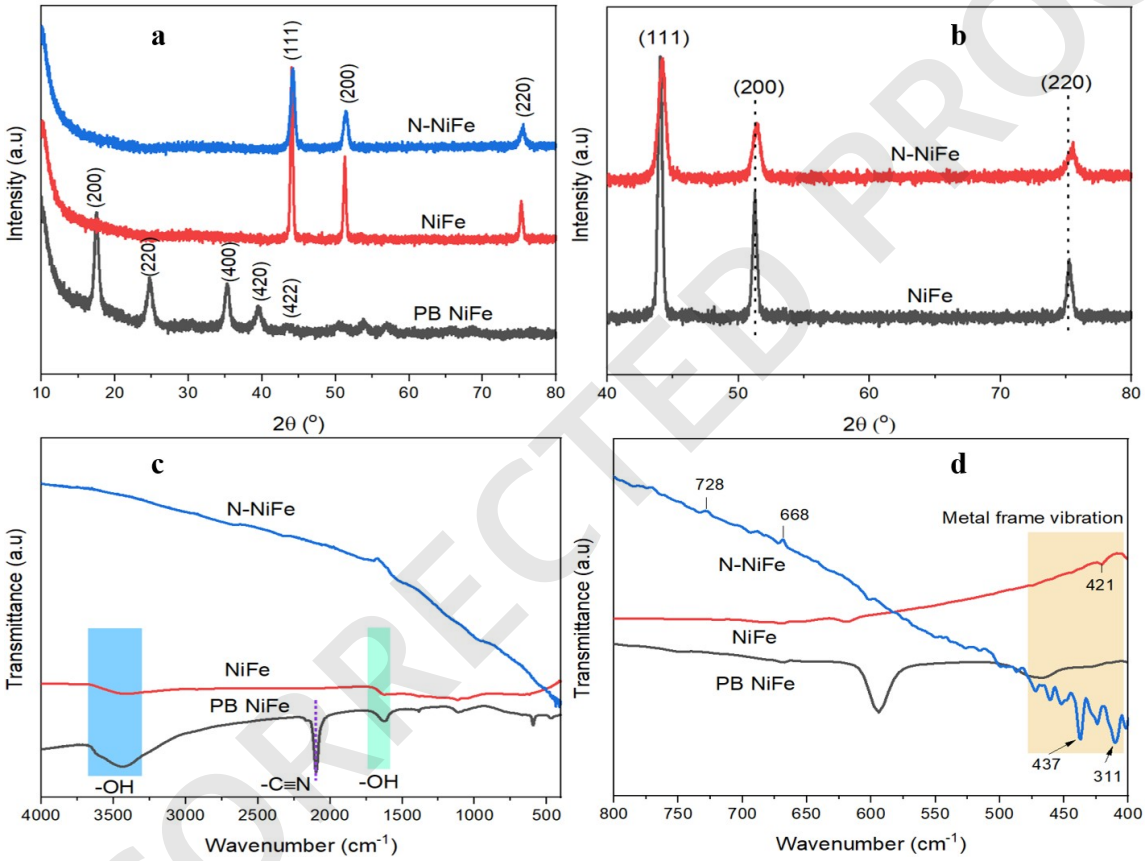

Figure 1. XRD patterns and FT-IR spectra of PB NiFe, NiFe, and N-NiFe (a, c) and a magnified view comparing NiFe and N-NiFe (b, d), respectively.

The IR spectra of PB NiFe and NiFe exhibit a broad, strong band in the 3440–3430 cm^{-1} region, characteristic of O–H stretching vibrations (H–O–H), and a narrower, weaker band at 1632–1626 cm^{-1}, assigned to O–H bending vibrations (H–O–H). This confirms the presence of adsorbed water molecules and coordinated water within structure of these materials [23].

The surface morphology of the materials was examined by SEM, as shown in Figure 2. The results reveal significant changes in morphology and surface structure between the initial PB sample and the post-thermal treatment samples.

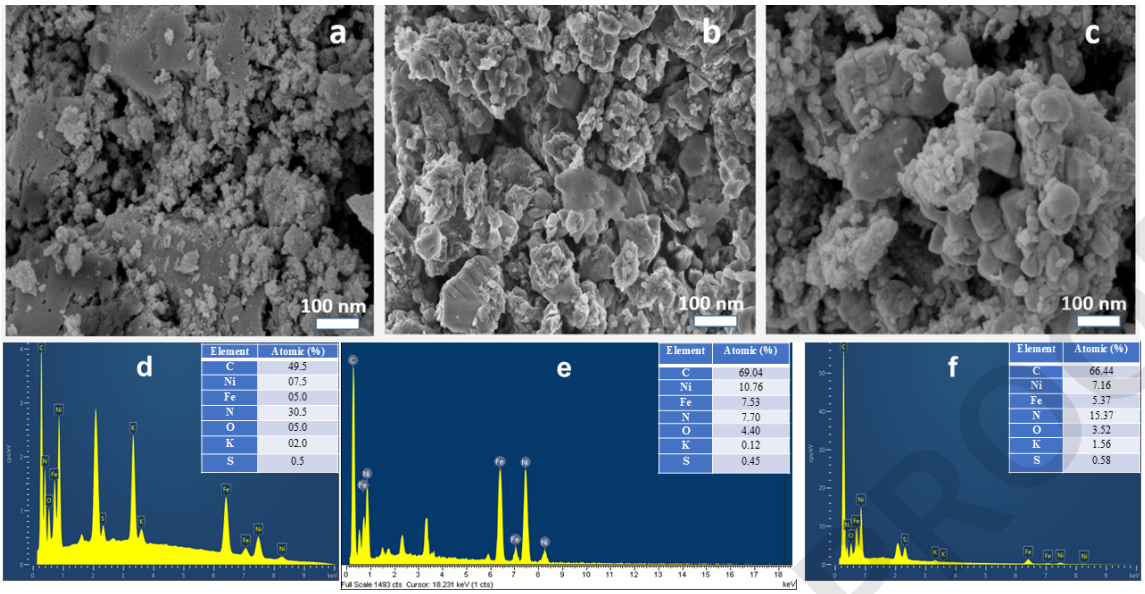

Figure 2. SEM images and EDS spectra of (a, d) PB NiFe, (b, e) NiFe, and (c, f) N-NiFe.

For PB NiFe, the SEM image (Figure 2a) shows small particles aggregated into porous clusters with a surface containing numerous pores and a loose, three-dimensional framework structure, typical of Prussian Blue Analogues. Figure 2b presents NiFe in the particles exhibiting a tendency to grow into larger, polyhedral shapes with higher crystallinity, consistent with the characteristics of a metallic NiFe alloy phase, which typically has a rough surface but a lower pore density compared to the PBA-derived precursor. This indicates that the calcination process reduces porosity and surface area. However, nitrogen doping may induce the formation of clusters, including the smaller particles observed in Figure 2c. This nitrogen-induced surface reconstruction can affect the catalytic activity of the material. The elemental composition of the samples was further confirmed by energy-dispersive X-ray spectroscopy (EDS) (Figure 2). As shown in Figure 2d, PB NiFe exhibits distinct peaks corresponding to Ni, Fe, C, and N, confirming the existence of the Ni–Fe cyanide framework derived from Prussian Blue. For the NiFe alloy sample, Figure 2e shows strong signals only for Ni and Fe, with no nitrogen peak, demonstrating the formation of a pure NiFe alloy phase. In contrast, the N–NiFe sample (Figure 2f) clearly shows a higher N content compared to the pristine alloy, confirming the successful incorporation of nitrogen into the alloy lattice. The results indicate that the molar ratio of Ni to Fe across all three samples is approximately 3:2. The presence of oxygen in all three samples is attributed to absorbed oxygen on surface, a common phenomenon for NiFe-based catalysts.

3.2. Electrocatalytic properties for HER

3.2.1. Linear sweep voltammetry

In principle, materials achieving higher current densities at lower electrode potentials signify superior catalytic performance, as a lower HER overpotential indicates a more facile water electrolysis process with lower energy consumption.

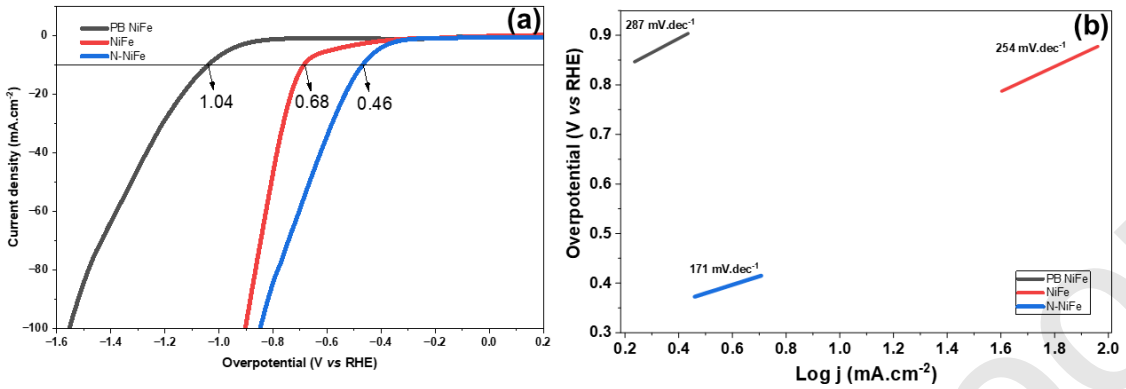

Figure 3. (a) LSV curves and (b) Tafel plots for the PB NiFe, NiFe, and N-NiFe catalysts in 0.5 M H_2SO_4, measured on a glassy carbon (L-shape) working electrode.

Figure 3a presents the linear sweep voltammetry (LSV) polarization curves for PB NiFe, NiFe, and N–NiFe. At a current density of 10 mA cm^{-2}, the required potential decreases in the order: PB NiFe (–1.04 V) > NiFe (–0.68 V) > N-NiFe (–0.47 V), demonstrating that N-NiFe possesses the highest electrochemical activity. This result indicates that nitrogen doping significantly reduces the activation energy and enhances the electron transfer rate, thereby improving the HER performance. This can be explained by the modulation of the NiFe electronic structure upon N-doping, which increases electron density around the Ni/Fe active centers and creates defect sites favorable for the adsorption of the H* intermediate. Simultaneously, the incorporation of N atoms into the crystal lattice enhances electrical conductivity and expands the electrochemically active surface area (ECSA), facilitating a more efficient reaction [24]. In contrast, the PB NiFe material, despite its open framework structure which facilitates uniform distribution of active sites, suffers from poor electrical conductivity, leading to inferior performance [15].

The Tafel slope, the one of the linear region, directly reflects the kinetic rate. A smaller slope value indicates that the catalyst requires less energy to achieve high current density, and thus possesses better HER performance. Figure 3b reveals slopes of 171 mV dec^{-1} (N-NiFe), 254 mV dec^{-1} (NiFe), and 287 mV dec^{-1} (PB NiFe), confirming that the HER kinetics are fastest for the N-NiFe sample. The smallest Tafel slope suggests favorable proton adsorption and reduction kinetics, where the H_2 release step is facilitated by the electron-rich catalytic surface. Both LSV and Tafel results confirm that nitrogen doping significantly optimizes the electrochemical performance of the NiFe alloy, reducing the overpotential and accelerating the reaction rate, promising effective application in HER/water electrolysis catalysis.

To further substantiate the superior HER performance of N-NiFe, the electrochemical active surface area (ECSA) was evaluated via cyclic voltammetry. The change in current density ΔJ (mA cm^{-2}) with respect to scan rate (mV s^{-1}) for each material was analyzed, where the slope of the linear fit represents the double-layer capacitance (Cdl, mF cm^{-2}). Since Cdl is proportional to the ECSA, it can be qualitatively described by the Cdl value [25]. The Cdl value reflects the electrode's charge storage capacity and is directly related to the number of electrochemically active sites on the surface. Therefore, a larger Cdl implies a greater charge storage capacity and a higher density of electrochemically active sites.

The cyclic voltammetry (CV) scans for the three materials recorded in the non-faradaic potential region at scan rates ranging from 5 to 200 mV s^{-1} are presented in Figures 4a-c. The

potential window investigated was from 0.05 V to 0.17 V (vs. RHE), with current densities ranging from –2.0 to 1.4 mA cm^{-2}. For PB NiFe (Figure 4a), the CV curves appear nearly linear, and the background current increases slightly with increasing scan rate, indicating a relatively low surface charging capacity and a limited number of electrochemically active sites (ECSA). This phenomenon is characteristic of Prussian Blue analogue materials, which typically exhibit poor conductivity and a crystalline structure not fully activated in the electrolyte environment [26]. For NiFe (Figure 4b), the CV loop expands noticeably as the scan rate increases, demonstrating improved conductivity and charge transfer efficiency compared to PB NiFe. This change reflects the role of alloying in enhancing the electronic interaction between Ni and Fe and promoting surface redox processes. Notably, the N-NiFe sample (Figure 4c) exhibits the most expanded CV loops and significantly higher current values at the same scan rates, indicating that nitrogen doping has created numerous defects and active sites while increasing the material's conductivity and substantially improving its electrochemical activity.

Figure 4d shows that the Cdl of the three materials follow an increasing order: PB NiFe < NiFe < N-NiFe. Specifically, the Cdl values are 0.20, 0.53, and 2.44 mF.cm^{-2}, respectively, indicating that N-NiFe has a charge storage capacity and electrochemically active surface area nearly 12 times higher than that of the PB NiFe sample. These differences reflect the structural changes in the material after modification. This is further confirmed in Figure 4e, where the N-NiFe sample exhibits the largest ECSA, demonstrating its superior number of active sites. The primary reason is that nitrogen doping creates lattice defects and increases electron density around the Ni and Fe metal atoms, thereby improving electrical conductivity and leading to a significantly expanded electrochemically active surface area. Conversely, the PB NiFe sample has a relatively dense structure with fewer defects, limiting the contact area with the electrolyte, resulting in low Cdl and ECSA. This, once again, confirms that doping contributes to an increased density of active sites and improved charge storage capacity, thereby facilitating the HER catalysis process.

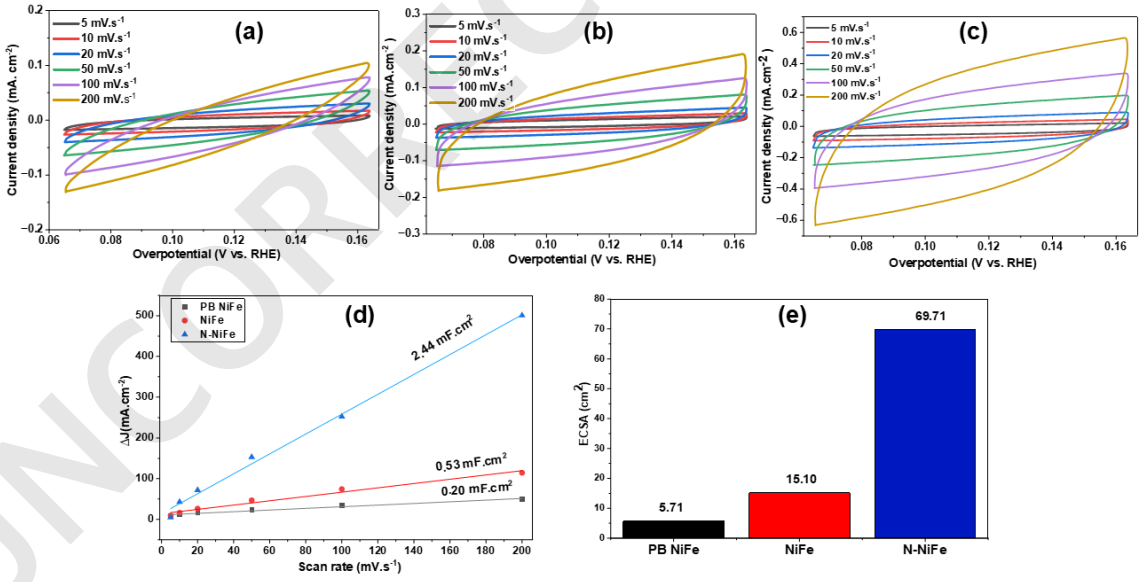

Figure 4. Cyclic voltammetry curves of (a) PB NiFe, (b) NiFe, and (c) N-NiFe; (d) double-layer capacitance (Cdl); and (e) electrochemically active surface area of PB NiFe, NiFe, and N-NiFe.

4. CONCLUSIONS

In this study, we successfully synthesized two Prussian blue analogue derived materials, NiFe alloy and its nitrogen-doped counterpart, N-NiFe, via a simple thermal treatment. The N-NiFe material demonstrated superior electrochemical performance for the hydrogen evolution reaction compared to both the pristine PB NiFe source material and the undoped alloy, NiFe. Specifically, N-NiFe exhibited a low overpotential at 10 mA cm^{-2} and a small Tafel slope, confirming the crucial role of nitrogen doping in optimizing reaction kinetics and accelerating electron transfer. This performance enhancement stems from the combined effects of a stable crystal structure, improved charge storage capacity, and electron density redistribution induced by nitrogen doping. The obtained results indicate that nitrogen-doped NiFe alloy holds promise as a potential non-precious metal electrocatalyst for application in water electrolysis for hydrogen production. Furthermore, this work opens prospects for developing NiFe alloys modified by doping with other elements for clean energy applications.

Acknowledgements. This research is funded by Vietnam National Foundation for Science and Technology Development (NAFOSTED) under grant number 104.05–2024.09.

CRediT authorship contribution statement. Lam Thi Thuy Kieu: Investigation, Data curation. Nguyen Tu Quyen, Truong Ngoc Cam Khuyen, Nguyen Nhat Tuan: Investigation. Nguyen Duc Nhan: Investigation, Data curation. Phan Thi Thuy Trang: Data curation, Writing – original draft. Le Thi Thanh Lieu: Investigation, Data curation. Dinh Quoc Viet: Investigation. Vien Vo: Supervision, Conceptualization, Writing – review & editing. Nguyen Van Thang: Writing – review & editing, Supervision, Resources, Funding acquisition.

Declaration of competing interest. The authors declare that they have no known competing financial interests or personal relationships that could have appeared to influence the work reported in this paper.

REFERENCES

1. Seh Z. W., Kibsgaard J., Dickens C. F., Chorkendorff I., Nørskov J. K., Jaramillo T. F. – Combining theory and experiment in electrocatalysis: Insights into materials design. Science, **355** (2017) eaad4998. https://doi.org/10.1126/science.aad4998.
2. Liu G., Xu Y., Yang T., Jiang L. – Recent advances in electrocatalysts for seawater splitting. Nano Mater. Sci., **5** (2023) 101–116. https://doi.org/10.1016/j.nanoms.2020.12.003.
3. Zhai P., Zhang Y., Wu Y., Gao J., Zhang B., Cao S., Zhang Y., Li Z., Sun L., Hou J. – Engineering active sites on hierarchical transition bimetal oxides/sulfides heterostructure array enabling robust overall water splitting. Nat. Commun., **11** (2020) 5462. https://doi.org/10.1038/s41467-020-19214-w.
4. Zhang B., Zheng X., Voznyy O., Comin R., Bajdich M., García-Melchor M., Han L., Xu J., Liu M., Zheng L., et al. – Homogeneously dispersed multimetal oxygen-evolving catalysts. Science, **352** (2016) 333–337. https://doi.org/10.1126/science.aaf1525.
5. Zhang L., Wu H. B., Lou X. W. (David) – Metal–organic-frameworks-derived general formation of hollow structures with high complexity. J. Am. Chem. Soc., **135** (2013) 10664–10672. https://doi.org/10.1021/ja401727n.
6. Chen Z., Fei B., Hou M., Yan X., Chen M., Qing H., Wu R. – Ultrathin Prussian blue analogue nanosheet arrays with open bimetal centers for efficient overall water splitting. Nano Energy, **68** (2020) 104371. https://doi.org/10.1016/j.nanoen.2019.104371.
7. Yang H., Liu J., Chen Z., Wang R., Fei B., Liu H., Guo Y., Wu R. – Unconventional bi-vacancies activating inert Prussian blue analogues nanocubes for efficient hydrogen evolution. Chem. Eng. J., **420** (2021) 127671. https://doi.org/10.1016/j.cej.2020.127671.

8. Zhang H., Diao J., Ouyang M., Yadegari H., Mao M., Wang M., Henkelman G., Xie F., Riley D. J. – Heterostructured core–shell Ni–Co@Fe–Co nanoboxes of Prussian blue analogues for efficient electrocatalytic hydrogen evolution from alkaline seawater. ACS Catal., **13** (2023) 1349–1358. https://doi.org/10.1021/acscatal.2c05433.
9. Huang C.-L., Chuah X.-F., Hsieh C.-T., Lu S.-Y. – NiFe alloy nanotube arrays as highly efficient bifunctional electrocatalysts for overall water splitting at high current densities. ACS Appl. Mater. Interfaces, **11** (2019) 24096–24106. https://doi.org/10.1021/acsami.9b05919.
10. Li R., Zhao J., Liu B., Wang D. – Atomic distance engineering in metal catalysts to regulate catalytic performance. Adv. Mater., **36** (2023) 2308653. https://doi.org/10.1002/adma.202308653.
11. Yu X., Yu L., Wu H. B., Lou X. W. (David) – Formation of nickel sulfide nanoframes from metal–organic frameworks with enhanced pseudocapacitive and electrocatalytic properties. Angew. Chem. Int. Ed., **54** (2015) 5331–5335. https://doi.org/10.1002/anie.201500267.
12. Zhou F., Gan M., Yan D., Chen X., Peng X. – Hydrogen-rich pyrolysis from Ni–Fe heterometallic Schiff base centrosymmetric cluster facilitates NiFe alloy for efficient OER electrocatalysts. Small, **19** (2023) 2208276. https://doi.org/10.1002/smll.202208276.
13. Johll H., Kang H. C., Tok E. S. – Density functional theory study of Fe, Co, and Ni adatoms and dimers adsorbed on graphene. Phys. Rev. B, **79** (2009) 245416. https://doi.org/10.1103/physrevb.79.245416.
14. Shah S. A., Ji Z., Shen X., Yue X., Zhu G., Xu K., Yuan A., Ullah N., Zhu J., Song P., et al. – Thermal synthesis of FeNi@nitrogen-doped graphene dispersed on nitrogen-doped carbon matrix as an excellent electrocatalyst for oxygen evolution reaction. ACS Appl. Energy Mater., **2** (2019) 4075–4083. https://doi.org/10.1021/acsaem.9b00199.
15. Cao L.-M., Lu D., Zhong D.-C., Lu T.-B. – Prussian blue analogues and their derived nanomaterials for electrocatalytic water splitting. Coord. Chem. Rev., **407** (2020) 213156. https://doi.org/10.1016/j.ccr.2019.213156.
16. McCrory C. C. L., Jung S., Ferrer I. M., Chatman S. M., Peters J. C., Jaramillo T. F. – Benchmarking hydrogen evolving reaction and oxygen evolving reaction electrocatalysts for solar water splitting devices. J. Am. Chem. Soc., **137** (2015) 4347–4357. https://doi.org/10.1021/ja510442p.
17. Feng Y., Wang X., Dong P., Li J., Feng L., Huang J., Cao L., Feng L., Kajiyoshi K., Wang C. – Boosting the activity of Prussian-blue analogue as efficient electrocatalyst for water and urea oxidation. Sci. Rep., **9** (2019) 15965. https://doi.org/10.1038/s41598-019-52412-1.
18. Hwa K.-Y., Sharma T. S. K. – Nano assembly of NiFe spheres anchored on f-MWCNT for electrocatalytic reduction and sensing of nitrofurantoin in biological samples. Sci. Rep., **10** (2020) 12256. https://doi.org/10.1038/s41598-020-69125-5.
19. Farah A. M., Billing C., Dikio C. W., Dibofori-Orji A. N., Oyedeji O. O., Wankasi D., Mtunzi F. M., Dikio E. D. – Synthesis of Prussian blue and its electrochemical detection of hydrogen peroxide based on cetyltrimethylammonium bromide (CTAB) modified glassy carbon electrode. Int. J. Electrochem. Sci., **8** (2013) 12132–12146. https://doi.org/10.1016/s1452-3981(23)13250-0.
20. Gu Y., Park D.-H., Kim M.-H., Byeon J.-H., Lim D.-M., Park S.-H., Kim J.-H., Jang J.-S., Park K.-W. – NiFe layered double hydroxides synthesized based on solvent properties as anode catalysts for enhanced oxygen evolution reaction. Chem. Eng. J., **480** (2024) 147789. https://doi.org/10.1016/j.cej.2023.147789.
21. Danilova J. S., Avdoshenko S. M., Karushev M. P., Timonov A. M., Dmitrieva E. – Infrared spectroscopic study of nickel complexes with salen-type ligands and their polymers. J. Mol. Struct., **1241** (2021) 130668. https://doi.org/10.1016/j.molstruc.2021.130668.
22. Andris E., Navrátil R., Jašík J., Sabenya G., Costas M., Srnec M., Roithová J. – Detection of indistinct Fe−N stretching bands in iron(V) nitrides by photodissociation spectroscopy. Chem. A Eur. J., **24** (2018) 5078–5081. https://doi.org/10.1002/chem.201705307.
23. Khairy M., Mahmoud K. G., Rashwan F. A., El-Sagher H. M., Banks C. E. – Nanosized nickel hexacyanoferrate modified screen-printed electrodes as flexible supercabattery platforms: Influence of annealing temperatures and supporting electrolytes. J. Energy Storage, **46** (2022) 103872. https://doi.org/10.1016/j.est.2021.103872.

24. Ullah N., Khan N., Nsang G. E. O., Shah S. A., Ullah B., Sayyar R., Rahim A., Ullah N., Wang G., Chun O., et al. – All in one: NiFe alloy embedded in N-doped carbon enveloped carbon cloth fiber for exceptional overall water splitting. Nano Mater. Sci. (2025). https://doi.org/10.1016/j.nanoms.2025.04.003.
25. Qiu B., Cai L., Wang Y., Guo X., Ma S., Zhu Y., Tsang Y. H., Zheng Z., Zheng R., Chai Y. – Phosphorus incorporation into Co_9S_8 nanocages for highly efficient oxygen evolution catalysis. Small, **15** (2019) 1904507. https://doi.org/10.1002/smll.201904507.
26. Zhang M., Wu W., Wang Z., Xie G., Guo X. – Boosting water oxidation activity via carbon–nitrogen vacancies in NiFe Prussian blue analogue electrocatalysts. Colloids Interfaces, **7** (2023) 14. https://doi.org/10.3390/colloids7010014.